Boundary shear stress induced by raindrop impact

Contrainte de cisaillement due a l'impact de gouttes d'eau sur une nappe liquide

D. M. HARTLEY
Research Hydraulic Engineer,
Hydro-Ecosystems Research Group,
USDA-Agricultural Research Service,
Fort Collins, CO 80522, USA

P. Y. JULIEN
Associate Professor of
Civil Engineering,
Colorado State University,
Fort Collins, CO 80523, USA

SUMMARY
An efficient mathematical model for calculation of the boundary shear stress field induced by raindrop impact is developed and tested using numerical and experimental data. The model comprises a series of dimensionally consistent, closed-form, algebraic equations, written in terms of physically meaningful parameters describing the fluid properties and initial conditions at the instant of drop impact. The relationships in the model are derived from the analysis of data generated by a computer code which numerically solves the Navier-Stokes equations for two-dimensional flow of a viscous, incompressible fluid with a free surface. The resulting simplified, algebraic model is validated using data from laboratory experiments which employ hot-film anemometry to measure drop induced boundary shear stresses. Substantial agreement is found between model and experimental results with regard to the boundary shear stress magnitudes and sensitivity of magnitudes to different water layer depths, drops sizes, drop velocities and distances from the center of drop impact.

RÉSUMÉ
Un modèle mathématique de calcul de contraintes de cisaillement lors de l'impact de gouttes d'eau sur une nappe liquide est développé et vérifié à l'aide de données numériques et expérimentales. Le modèle consiste en une série d'équations algébriques en function des principaux paramètres physiques décrivant l'impact de gouttes d'eau. Les relations du modèle sont basées sur une analyse de données obtenues par une solution numérique des équations de Navier-Stokes appliquées à l'analyse bi-dimensionnelle d'un écoulement visqueux incompressible lors d'un impact de gouttes d'eau sur une nappe liquide. Le modèle algébrique simple qui en résulte est validé à partir de données de contraintes de cisaillement mesurées en laboratoire à l'aide d'une technique anémométrique à film chaud. Il existe un bon accord entre le modèle et les mesures expérimentales relativement à l'amplitude des contraintes de cisaillement ainsi que la sensibilite du modèle aux paramètres tels la taille et la vitesse des gouttes d'eau, la profondeur de la nappe d'eau et la distance du point d'impact.

1 Introduction

The deformation of a liquid surface struck by a droplet was first photographed and studied systematically by Worthington (1882) at the end of the 19th century. His classic monograph (1908), republished posthumously just a few decades ago (1963) described experiments involving droplet impact on both dry, smooth surfaces and deep liquid pools. Worthington was primarily concerned with the evolution of the splash structure as affected by droplet impact velocity and surface tension. Later, Laws (1939, 1940) applied high-speed motion picture photography techniques to the study of raindrop splashes on soil covered by thin layers of water. He identified the lateral jet of the expanding splash crater and the ejection of numerous droplets from the splash

Revision received March 1, 1991. Open for discussion till December 31, 1992

crown as mechanisms of soil particle detachment and transport. Photographs from this study show that when a large drop strikes a water layer, a crater expands horizontally over a period of approximately 35 msec and collapses over a period twice that long. The vertical motion forming the cylindrical shell of the splash crown is superimposed on this horizontal motion. The rise of the shell occurs over approximately 1/5 and the collapse over 4/5 of the cycle.

Other investigators (Hobbs and Kezweeny, 1967; Hobbs and Osheroff, 1967; Macklin and Hobbs, 1969; Mutchler and Hansen, 1970; Macklin and Metaxes, 1976) used photographs to correlate various aspects of drop morphology such as crown droplet formation, crater shape, maximum crater size and height of the recoil jet with initial conditions such as drop size, impact velocity and pool depth. Macklin and Hobbs (1969) observed that when a 2.3 mm drop impacted a pool with a depth greater than 4 drop diameters at about 50% of terminal velocity, a hemispherical crater formed and fluid motion was predominantly vertical. At depths less than 2.5 drop diameters, the splash crater contacted the bed and became conical in shape. At the shallowest depths, the crater was cylindrical and fluid motion was predominantly horizontal. Mutchler and Hansen (1970) found that splash diameter and height increased from zero to a maximum as pool depth increased from zero to 1/3 drop diameters. These splash dimensions decreased as pool depth increased from 1/3 to 3 drop diameters, and then remained constant for depths greater than 3 diameters. Later Mutchler and Young (1975) used Mutchler and Hansen's data to develop empirical relationships for crater expansion rates and infer rough estimates of the variation of bed shear with time after drop impact. They also suggested that water depths greater than 3 drop diameters were sufficient to protect the soil surface from raindrop action. This rule of thumb was based on the observation of the invariance of splash size with pool depth at depths greater than 3 drop diameters and the hypothesis that forces on the bed would be negligible under these conditions.

Both analytical and numerical studies have complemented experimental research into the dynamics of the drop impact phenomenon. Engel (1966) derived an energy balance for the instant of maximum crater size and derived an expression for the maximum crater radius which compared well with experimental data. At about the same time, numerical simulations of the drop impact problem were being performed which provided both synthetic pictures of dynamic splash morphology and evaluation of the dynamic pressure and velocity fields within the fluid. Harlow and Shannon (1967) used the MAC or "Marker and Cell" (Welch at al., 1965) technique to numerically solve the Navier-Stokes equation for drop impact on a free surface. Their simulations were restricted to low velocity impact in the absence of surface tension and viscosity. For these conditions, the simulation showed that the drop material tended to line the bottom and sides of the crater.

Wang (1970) modified the model used by Harlow and Shannon and applied it to more realistic drop impact conditions which included surface tension and viscous forces. Wang's objective was to numerically investigate the pressure field generated by single drop impacts on shallow pools with drop sizes and velocities similar to those found in natural rainfall. Using results of numerical simulations, Wang developed an equation describing peak pressure on the boundary as a function of the drop stagnation pressure at impact and a ratio of drop size to pool depth. This equation agreed well with experimental data obtained with a pressure cell. He found that boundary pressure generally built up to a maximum within 1.0 msec and that at the instant of peak pressure, the spatial distribution of the pressure was Gaussian and centered on the axis of impact. Wang made a few rough calculations of peak shear based on simulated velocity differences between computional cells adjacent to the lower boundary but the computational grid was too coarse to allow a good estimate of the velocity gradient.

Further numerical simulation using the MAC method was carried on by Huang et al. (1982) for drop impacts in the absence of viscosity and surface tension. They found that a 4.0 mm drop impacting a solid surface produced pressures lasting a few microseconds which were 20 times the stagnation pressure and that radial jet velocities were twice the impact velocity. More recently, Tan (1990) reviewed many of the experimental and numerical studies of raindrop splash and erosion. He also proposed a raindrop erosion model which suggested that erosive pressures on the soil surface are maximized when a water layer equal to the drop diameter is present.

2 Focus and methodology

This study focuses on the boundary shear stress induced by raindrop impact on layers of water which are less than 3.0 raindrop diameters because past research indicates that erosive forces become practically insignificant at larger water depths (Wang, 1970; Mutcher and Young, 1975). Additionally, analysis is confined to the initial period of drop penetration and crater expansion when drop momentum is concentrated in a relatively small area around the impact site. During this period, pressure gradients, fluid velocities and boundary shear stresses are large in comparison to later stages of splash (Worthington, 1963; Laws, 1939; Wang, 1970; Harlow and Shannon, 1967).

Based on physical considerations and a dimensional analysis, Hartley (1990) showed that a general equation for the time and space varying boundary shear stress field can be written in terms of a Reynolds number R, Weber number W, Froude number F, dimensionless pool depth y_0^* and dimensionless space and time values x^* and t^* as follows:

$$\tau^* = f(R,\ W,\ F,\ y_0^*,\ x^*,\ t^*) \tag{1}$$

in which $\tau^* = \tau/\varrho V_0^2$, $R = \varrho V_0 r/\mu$, $W = \varrho V_0^2 r/\sigma$, $F = V_0/(gr)^{0.5}$, $y_0^* = y_0/r$, $x^* = x/r$, and $t^* = V_0 t/r$. Here τ is the boundary shear stress, ϱ is the fluid density, V_0 is drop impact velocity, r is the radius of the drop, μ is the fluid dynamic viscosity, σ is the surface tension, g is the gravitational acceleration, y_0 is the initial depth of the pool at the instant of impact, x is the radial distance from the vertical axis of symmetry and t is the time since the instant of impact. As noted by Harlow and Shannon (1967), gravity and surface tension forces both tend to restore the water surface to a horizontal or rest position. Numerical simulations conducted by Hartley (1990) corroborated this analysis and lead to the simplification of equation (1) by merging F and W into a single parameter θ as follows:

$$\tau^* = f(R, \theta, y_0^*, x^*, t^*) \tag{2}$$

in which

$$\theta = F W^{0.5}/(F + W^{0.5}) \tag{3}$$

This simplification is justified by Hartley's results which showed a similar sensitivity of the boundary shear stress field to F and $W^{0.5}$ when either or both parameters were small. This trend is represented by equation (3). Additionally, it is shown in the following analysis that gravity and surface tension forces have only a minor effect on shear stress magnitudes.

Equation (2) describes drop induced boundary shear stress in terms of dimensionless variables which use the drop impact velocity and drop radius as space and time scaling factors. The functional dependence of the dimensionless boundary shear stress on the independent dimensionless variables defined in equation (2) was investigated using a numerical solution to the equations of

fluid motion. A set of empirical relationships for the boundary shear stress was developed from the results of the numerical experiments. Subsequently, the numerically derived empirical relationships were compared with results from laboratory experiments.

3 Numerical model

The numerical model employed in this study is a modified version of the SOLA-VOF model (Nichols et al., 1980). SOLA-VOF is a generic code for the finite difference solution of two-dimensional, viscous, incompressible flow problems involving free surfaces or boundaries between two immiscible fluids. Particular flow problems are defined through the specification of appropriate boundary and initial conditions by the code user. Consequently, SOLA-VOF has been applied to a wide range of flow problems (Nichols et al., 1980) including a jet impinging on a wall, collapse of a tank surrounded by a retaining wall, and instability of a thin liquid column due to surface tension. Additionally, Hartley (1990) validated the model's ability to solve unsteady viscous flow problems by comparing simulation results with the analytical solution for the problem of a suddenly accelerated plate in an unbounded fluid medium.

The basic numerical procedure used to solve the equations of motion by SOLA-VOF employs an explicit difference scheme to obtain estimates of the entire velocity field at the advanced time step. These velocities are checked by computing the divergence or error in continuity which in turn is used to correct pressure values throughout the domain. Velocities are recomputed and the iterations continue until the divergences at all locations are smaller than a user-defined tolerance. Unlike earlier hybrid Eulerian-Lagrangian techniques such as the MAC method (Welch et al., 1965) which used massless marker particles to track the movement of free surfaces, SOLA-VOF is purely Eulerian. Fluid interfaces or free surfaces are tracked using a step function which defines the presence or absence of fluid at a point. Details of this method and other features of the numerical solution employed by SOLA-VOF are presented elsewhere (Nichols et al., 1980; Hirt and Nichols, 1981) and will not be repeated here. Hartley (1990) and Hartley and Alonso (1990) discuss modifications of the SOLA-VOF code and its application to the problem of raindrop impact.

4 Simulation experiments

A set numerical experiments was conducted using the modified SOLA-VOF numerical code described by Hartley (1990) in which the dependence of the dimensionless boundary shear stress on the independent variables identified in equation (1) was investigated. Numerical simulation of natural raindrop conditions was considered desirable, but the large Reynolds numbers of these drops required prohibitively small computional cells and time steps to define boundary layers and maintain numerical stability (Hartley, 1990). Thus, simulations were conducted at lower Reynolds numbers than occur during the impact of natural raindrops. Table 1 compares Reynolds number and other parameter values for natural raindrops and the laboratory and numerical simulation conditions of this study.

Fig. 1 represents typical results of the numerically calculated boundary shear stress field. As shown in the figure, the boundary shear stress field can be described by a family of curves in which each curve represents the spatial distribution of the boundary shear stress at a particular instant in time. In this study, "peak boundary shear stress" (τ_p) refers to the peak of a spatial distribution at an instant in time (i.e. peak of any curve in Fig. 1) while "maximum peak boundary

Table 1. Comparison of parameters ranges

parameter	natural rainfall[1]	laboratory experiment	computer simulations
R	6500. - 23000.	1600. - 7700.	50. - 500.
y_0^*	0.00 - infinity	0.88 - 5.00	0.50 - 6.00
θ	18.0 - 28.0	3.1 - 10.1	2.8 - 22.6

[1] Raindrop diameters assumed to range from 2.0 mm to 5.0 mm.

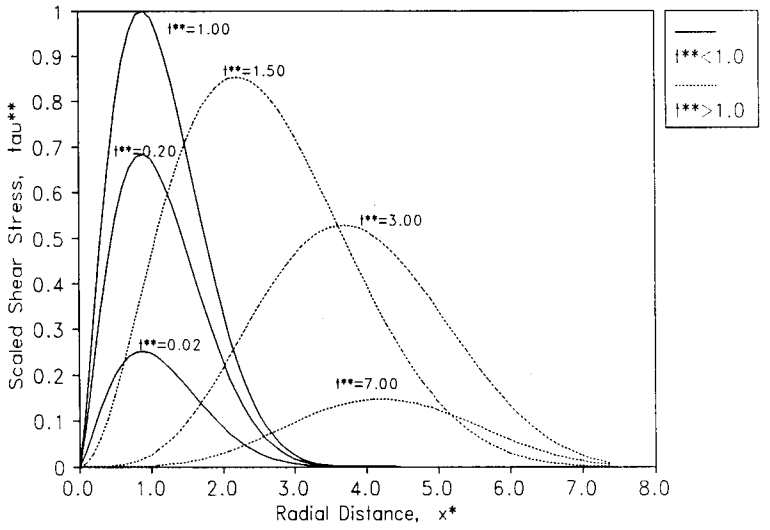

Fig. 1. Typical simulated boundary shear stress distributions at different times after drop impact.
Distributions typiques des contraintes de cisaillement simulées à différents intervalles de temps après impact.

shear stress" ($\tau_{p\,max}$) refers to the global maximum or largest of the peaks (peak value of distribution represented by bold line in Fig. 1) The double asterisk superscript (τ^{**}) on the y-axis of Fig. 1 denotes boundary shear stress magnitudes normalized by the magnitude of the maximum peak boundary shear stress ($\tau_{p\,max}$) while the time labels above the curves (t^{**}) indicate time values scaled by the time to reach the maximum boundary shear stress magnitude ($t_{p\,max}$).
Although details of the pattern vary depending on values of controling parameters, the trend shown in Fig. 1 is typical. That is, the rise to maximum shear was generally quite rapid (curves with solid lines) in comparison with a longer period of shear decay (curves with dashed lines). Also, prior to the time of the maximum boundary shear stress ($t^{**} < 1.0$), spatial distributions of the shear tended to be geometrically similar and spatially concurrent. During the relatively extended period of decay (dashed curves) the shear tended to diffuse further from the center of impact and to become more symmetrically distributed. Fig. 2 shows how shear magnitudes varied in time by plotting peak values from the curves in Fig. 1 and simply reinforces the point that the entire shear pulse reaches a maximum value within a very short period compared to duration of the entire pulse.

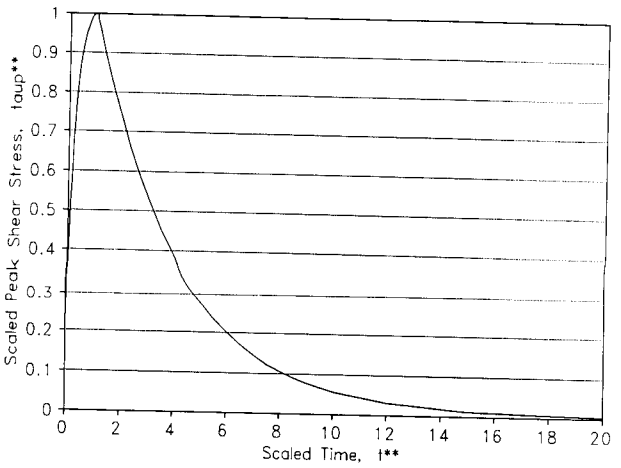

Fig. 2. Typical simulated temporal variation in magnitude of peak shear stress.
Variation temporelle typique des pointes de cisaillement simulées.

5 Simplified equations for the boundary shear stress field

In order to arrive at a set of simplified algebraic equations which could be used to generate the dynamic boundary shear stress field represented in Fig. 1, the entire numerically generated data set was analyzed and various functions of the independent variables in equation (2) were optimized using a nonlinear optimization routine (DeCoursey and Snyder, 1969). As a result of this analysis, it was found that the boundary shear stress distributions at various instants in time could be well-approximated by beta functions. Additionally, these beta functions remained constant in shape and range prior to the instant of maximum peak shear but change shape and range thereafter. Detailed discussion and comparison of individual equations with numerical model results are given by Hartley (1990). A summary of the relationships which make up the algebraic model are presented below.

5.1 *Maximum peak boundary shear stress*

The variation in magnitude of the maximum peak boundary shear stress ($\tau^*_{p\,max}$) was studied using the numerical model over a range of the dimensionless parameters identified above. Results of these simulations are given in Table 2. Simulated maximum peak boundary shear stress declined steeply with increased water layer depth. For example, maximum peak boundary shear stresses at depths of 6.0 radii were only about one percent as large as at a depth of 0.50 radii. This agrees qualitatively with the suggestion of Mutchler and Young (1975) that a depth of 6.0 radii would protect the soil surface from erosion. Wang (1970) noted a similar dramatic reduction in maximum peak boundary pressure with increasing water layer depth in his raindrop splash study. Evidently, both the pressure and shear stress attenuation reflect the cushioning effect of the water layer.

Simulated maximum peak boundary shear stresses also consistently declined with Reynolds number. This trend is similar to the one reported by Rajaratnam (1976) for peak boundary shear stress caused by an impinging circular jet, a steady flow case which is quite simular to drop impact. There was also a small effect of gravity and surface tension over the range of numerically simulated conditions.

Table 2. Modified SOLA-VOF simulation of maximum peak boundary shear stress

run#	y_0^*	R	θ	$\tau^*_{p\,max}$
1	0.50	50	3	7.900E-02
2	0.50	50	6	7.227E-02
3	0.50	50	12	7.083E-02
4	0.50	50	24	6.960E-02
5	1.00	50	3	4.505E-02
6	1.00	50	6	3.838E-02
7	1.00	50	12	3.454E-02
8	1.00	50	24	3.454E-02
9	1.00	150	3	2.562E-02
10	1.00	150	6	2.052E-02
11	1.00	150	12	1.847E-02
12	1.00	150	24	1.741E-02
13	1.00	500	3	1.446E-02
14	1.00	500	6	1.133E-02
15	1.00	500	12	9.296E-03
16	1.00	500	24	9.296E-03
17	2.00	50	3	1.171E-02
18	2.00	50	6	1.271E-02
19	2.00	50	12	1.271E-02
20	2.00	50	24	1.271E-02
21	2.00	150	3	6.038E-03
22	2.00	150	6	6.793E-03
23	2.00	150	12	6.793E-03
24	2.00	150	24	6.793E-03
25	2.00	500	3	2.760E-03
26	2.00	500	6	3.240E-03
27	2.00	500	12	3.240E-03
28	2.00	500	24	3.140E-03
29	4.00	50	3	1.820E-03
30	4.00	50	6	2.000E-03
31	4.00	50	12	2.484E-03
32	4.00	50	24	2.484E-03
33	4.00	150	3	8.172E-04
34	4.00	150	6	1.124E-03
35	4.00	150	12	1.330E-03
36	4.00	150	24	1.328E-03
37	4.00	500	3	2.900E-04
38	4.00	500	6	4.300E-04
39	4.00	500	12	5.143E-04
40	4.00	500	24	5.657E-04
41	6.00	50	3	5.430E-04
42	6.00	50	6	6.723E-04
43	6.00	50	12	7.499E-04
44	6.00	50	24	8.016E-04

However, for erosive natural rainfall conditions, sensitivity of the maximum peak boundary shear stress to the gravity and surface tension parameter would be negligible. Optimization using the numerically simulated data resulted in the following relationship:

$$\tau^*_{p\,max} = 2.85\,(y_0^* + 1)^{-3.16}\,R^{-.55}\,C_1 \tag{4}$$

with a coefficient of determination $r^2 = 0.99$. The term in parenthesis in this relationship is equal to the sum of the pool depth and drop radius scaled by the radius. The factor C_1 is defined by:

$$C_1 = [1.0 - \exp(-1.6\,\theta/y_0^*)] \tag{5}$$

It represents the effect of gravity and surface tension but deviates very little from a value of 1.0 for erosive natural rainfall conditions in which θ is generally larger than 9.0 and y_0^* less than 6.0. This suggests C_1 values ranging from .91 to 1.0 and supports the earlier contention that gravity and surface tension have a minor influence on the boundary shear stress.

5.2 *Time to reach maximum peak boundary shear stress*

Simulated values of the dimensionless time to reach maximum peak boundary shear stress $t^*_{p\,max}$, were found to be primarily a function of the dimensionless depth y_0^* and secondarily a function of θ, the combined gravity and surface tension parameter. The effects of gravity and surface tension appear to be small for low values of y_0^*, but much larger for larger depths. The variation of $t^*_{p\,max}$ with y_0^*, and θ can be described by the following optimized relationship (coefficent of determination $r^2 = 0.99$):

$$t^*_{p\,max} = 1.4\,(y_0^* + 1)\,C_2 \tag{6}$$

in which

$$C_2 = [1. - \exp(-.60\,\theta/y_0^*)] \tag{7}$$

Similar to C_1, the factor C_2 is of minor importance, varying between 0.88 and 1.0 for most cases of practical interest ($\theta > 18$ and $y_0^* < 5$). Thus, equation (6) indicates that the time interval between drop impact and maximum peak boundary shear stress is approximately proportional to the travel time at the impact velocity over a distance equal to the drop radius plus the pool depth - a physically reasonable result.

5.3 *Growth and decay of peak boundary shear stress*

Fig. 2 shows the typical numerical simulation results for the variation in peak boundary shear stress magnitudes with time. As shown in the figure, peak boundary shear stress magnitudes increased rapidly to a maximum value following impact. The rate of boundary shear stress growth depended mainly on the dimensionless depth y_0^* and could be represented by a gamma function (coefficient of determination $r^2 = 0.80$) as follows:

$$\tau_p^{**} = (t^{**})^{\gamma} \exp[\gamma(1. - t^{**})], \text{ for } t^{**} \leq 1.0 \tag{8}$$

Here the double asterisk superscripts indicated that the dimensionless time t^* has been scaled by the dimensionless time to reach the maximum peak $t^*_{p\,max}$ and the peak boundary shear stress τ_p^* has been scaled by the maximum peak boundary shear stress $\tau^*_{p\,max}$. The single parameter γ can be estimated by:

$$\gamma = 0.7\,(y_0^*)^{.55} \tag{9}$$

Equation (8) represents the initial part of the curve shown in Fig. 2 prior to the occurrence of the maximum peak boundary shear stress. The rate of decay of peak boundary shear stress magnitudes following the maximum peak was found to depend most strongly on gravity and surface tension forces as represented by the parameter θ. When θ was small, decay tended to be rapid, reflecting the restoring effect of gravity and surface tension forces. Conversely, when θ was large, decay of the peaks proceeded more slowly. The decay of peak boundary shear stresses could be described by the following exponential relationship (coefficient of determination $r^2 = 0.85$):

$$\tau_p^{**} = \exp - [\lambda_d (t^{**} - 1.)] \tag{10}$$

in which the λ_d is given by

$$\lambda_d = 1.35\,\theta^{.64} + .12. \tag{11}$$

λ_d varies from 0.33 to 0.28 for natural raindrops ranging in size from 2.0 to 5.0 mm in diameter. It may be taken as a constant at 0.31 for these conditions with less than a 20% deviation in τ_p^{**} for $t^{**}<8.5$. Thus, it can be seen that θ gains in importance as shear stress magnitudes subside, but may be neglected in the determination of the earlier, larger stresses under natural rainfall conditions.

5.4 *Spatial distribution of boundary shear stress*

The spatial distributions of boundary shear stresses at various instants during the growth and decay of boundary shear stress magnitudes was examined using the graphical output from the numerical model. Various distribution functions including gamma, lognormal, and beta distributions were fitted to the simulated boundary shear stress values. Nonlinear optimization results demonstrated that a beta distribution with a left boundary at the axis of impact did an excellent job of representing the finite difference results. The beta function is defined:

$$\tau^{**} = C_\beta\,(x^*/x_r^*)^{p1}(1 - x^*/x_r^*)^{p2} \tag{12}$$

in which τ^{**} is the boundary shear stress at any instant scaled by the maximum peak boundary shear stress, C_β is a beta constant, x^* is the radial distance from the axis of drop impact scaled by the drop radius, x_r^* is the right-hand boundary of the distribution and $p1$ and $p2$ are beta distribution shape parameters. The parameters of the distribution are C_β, *p1*, and *p2* and x_r^*. The first parameter controls the magnitude of the τ^{**} values, while the powers *p1* and *p2* control skewness and kurtosis. The following relationships among the beta parameters, the scaled peak magnitude τ_p^{**} and position x_p^* can be shown to hold identically:

$$p2 = p1\,(x_r^* - x_p^*)/x_p^*, \tag{13}$$

and

$$C_\beta = \tau_p^{**}\,(x_p^*/x_r^*)^{-p1}\,(1 - x_p^*/x_r^*)^{-p2}. \tag{14}$$

Finite difference model results were used to optimize relationships which completed the description of the spatial distribution of the boundary shear stress. For the period between the instant of impact and the occurrence of the maximum peak boundary shear stress ($t^{**} < 1.0$) the shape of the spatial distribution remained essentially constant and the following equations were found to produce an accurate facsimile of the finite difference results:

$$p1 = 1 + \exp(-1.25\,y_0^*), \tag{15}$$

$$x_r^* = 1 + 7.5\,[1 - \exp\,(-1.25\,y_0^*)], \tag{16}$$

$$x_p^* = .88 + 5\,\exp\,(-3.7/y_0^*). \tag{17}$$

Equations 15–17 together with identities 12–14 represent the spatial distribution of the boundary shear stress field for $t^{**} < 1.0$. These relationships fit the finite difference model results very closely ($r^2 > 0.95$) over the entire range of conditions simulated. An example of the fit between these equations and the finite difference model is shown in Fig. 3 in which the solid lines

represent the equations and the symbols represent finite difference model results for $t^{**} \leqq 1.00$. These results indicate that according to the model, the dimensionless depth y_0^* is the only parameter controlling the spatial distribution during the period of boundary shear stress build-up to the maximum peak boundary shear stress.

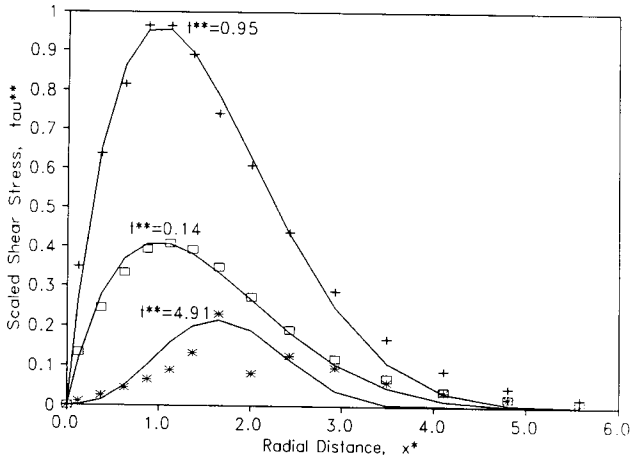

Fig. 3. Typical comparison of algebraic and numerical results.
Comparaison typique des résultats des modèles algébrique et numérique.

For period of shear decay ($t^{**} > 1.0$), equations 15–17 are replaced by

$$x_{pd}^* = x_p^* \{1. + (.21\,\theta - 20.\,R^{-0.5}) \cdot \exp[-y_0^*/(t^{**} - 1)]\} \tag{18}$$

$$p1_d = p1 + (p2 - p1) \exp[-1./(t^{**} - 1.)] \cdot \exp(-.30 y_0^{*2}) \tag{19}$$

$$p2_d = p2 \tag{20}$$

and

$$x_{rd}^* = x_{pd}^* (p2_d/p1_d + 1) \tag{21}$$

All variables are as previously defined. The subscript d is added to the parameters to show that they apply to decay period. For this period, the optimization of the equations (12–14 plus 18–21) to the finite difference model results in $r^2 > 0.85$ over the range of simulation conditions given in Table 2. While still good, this fit is inferior to the earlier period of shear build-up. Also in contrast to the earlier period, dimensionless time t^{**} and the parameters θ and R affect the spatial distribution of the shear. An example of the fit between the equations and the finite difference model is shown by the $t^{**} = 4.91$ in Fig. 3.

Equations (1) through (21) provide a complete algebraic description of the boundary shear stress field during the period of splash crater expansion. In summary, the boundary shear stress field simulated with the finite difference model can be approximated from the drop radius r, the impact velocity V_0, the pool depth y_0^* and the physical constants ϱ, ν, σ and g.

6 Experimental validation of the algebraic model

The set of approximate equations for estimation of the boundary shear stress field were tested using laboratory data collected with a hot-film anemometry system. In these tests water drops of various sizes and velocities were imposed upon low velocity flows in a rectangular flume. Boundary shear stress pulses caused by the drops were measured using a flush-mounted, hot-film boundary shear stress probe.

6.1 *Methods and materials*

Laboratory experiments were conducted in a 0.21 m wide by 9.75 m long rectangular flume using filtered and deionized water which was maintained at a constant temperature. A schematic of the experimental equipment is shown in Fig. 4. The probe with a 0.25 by 1.00 mm hot-film sensor was mounted so that the sensor was flush with the bed of the flume. The probe was connected by a cable to a constant temperature anemometer. The anemometer is designed to supply sufficient power to the hot-film sensor to maintain it at a constant temperature. Voltage output from the anemometer indicates the instantaneous boundary shear stress on the sensor through a well defined calibration relationship (Sandborn, 1972). Anemometer voltage output was automatically stored in a minicomputer.

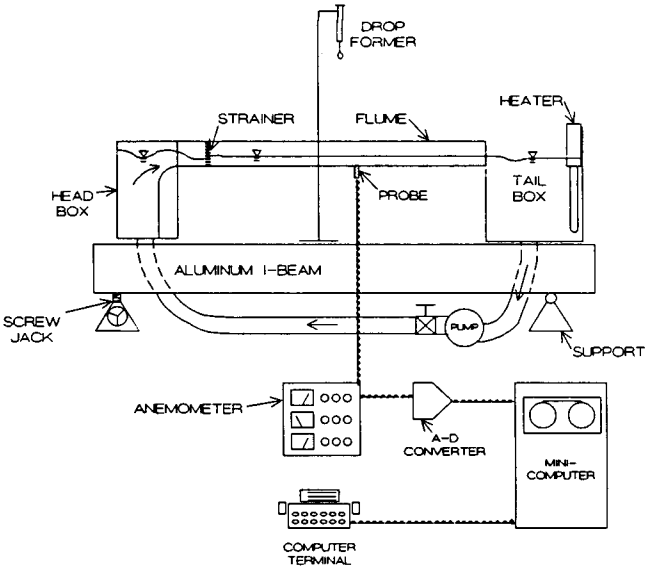

Fig. 4. Schematic of experimental setup.
Schema des conditions expérimentales.

Water droplets were formed using a hypodermic syringe. Three drop diameters were used: 3.2, 3.8 and 4.5 mm. The two smaller drop sizes were generated using hypodermic needles with the points cut off and ends filed. The largest drop size was generated using the plastic syringe without an attached needle. Gravimetric tests verified that drops generated using these orifices were quite uniform with sample standard deviations of approximately 1% of the nominal size. The syringe

was attached to a ring stand at a location designed to produce impact at a specified distance from the hot-film sensor and at a known impact velocity.
The flush mount hot-film sensor obeys the standard calibration relationship (Sandborn, 1972):

$$\tau^{1/3} = A E^2 - B \tag{23}$$

in which τ is the instantaneous boundary shear stress, E is the anemometer voltage output and A and B are constants which must be determined by calibration. The calibration constants are sensitive to water temperature and can also be effected by water quality which is the reason for using temperature controlled, filtered and deionized water in the experiments. These features of the measurement system are discussed in more detail by Schall (1979). The constants A and B must be determined using a flow with a known boundary shear stress value. This was accomplished by establishing uniform flow in the laboratory flume over the range of slopes and flow depths and estimating the average boundary shear stress using the relationship:

$$\tau = \gamma y S \tag{24}$$

in which τ is the time average boundary shear stress, γ is the specific weight of water, y is the flow depth and S is the friction slope which is equal to the slope of the flume bed for uniform flow conditions.
Measurements of boundary shear stress pulses caused by impacting water drops were designed to investigate effects of water layer depth, drop impact velocity, drop size and distance from the point of drop impact. Ranges of experimental variables are shown in Table 3 and the resultant range of dimensionless variables are shown in Table 4.

Table 3. Range of dimensional variables investigated

variable	values
water depth, y_0	2.0, 4.0, 6.0, 8.0 mm
drop impact velocity, V_0	1.0, 1.7, 3.4 m/s
drop diameter, d	3.2, 3.8, 4.5 mm
distance from impact, x	5.0, 10.0, 15.0 mm

All drop induced boundary shear stress pulse measurements were conducted with a small uniform discharge flowing in the flume. The presence of a base flow was considered necessary in order to maintain constant temperature of fluid over the hot-film sensor. Base flows were in the laminar to transitional range ($100 < Re < 1200$) and velocities were small ($0.05 < V_x < 0.17$ m/s). Hartley (1990) used a force balance to demonstrate that the base flows have a negligible effect on the boundary shear stress measurements because of the comparitively short duration of the shear stress pulses.
After daily calibration runs, the flume slope was set at .004 and flow rate was adjusted until the desired uniform flow depth was achieved. A ring stand was used to position the water drop former at a height which would result in the proper drop impact velicity. This height was determined using the method presented by Wang (1970). The horizontal position of the drop former was adjusted by sight and touch with the aid of a 2.0 mm diameter plastic rod. Drop impacts were sited within 1.0 mm of the desired impact point with this method. When the drop former was located at the proper location, static head was adjusted on the drop former so that drops fell at approximately 2.0 seconds intervals. This rate guaranteed that boundary shear stress pulses from

successive drops would be independent. When the desired rate of drop impacts had been achieved, the anemometer output was sampled for 10 seconds at a frequency of 1000 hertz (1-2% of the cut-off frequency of the system) and 4 to 5 replicate boundary shear stress pulses were recorded.

Table 4. Range of dimensionless variables investigated

variable	range
dimensionless depth, y_0^*	0.88 - 5.00
Reynolds number, R	1600 - 7700
gravity-surface tension parameter, θ	3.1 - 10.1
dimensionless distance, x^*	2.22 - 9.38

6.2 *Comparison of algebraic model and experimental data*

The previously described algebraic model for the boundary shear stress field was used to simulate boundary shear stress pulses corresponding to the experimental conditions. Comparisons of model and experimental results are summarized in Figs. 5 through 7. Fig. 5 compares results of the model and experiments at three different flow depths for a period of 50 msec. As indicated by Fig. 5, the model generally follows the trend in the experimental data of decreasing boundary shear stress peaks with flow depth. At the 2.0 mm depth, the model estimates a boundary shear stress peak which is nearly twice as large as the measured value. However, it should be noted that estimated inaccuracies in the setting of flow depth and positioning the drop impact point would be sufficient to account for this discrepancy.

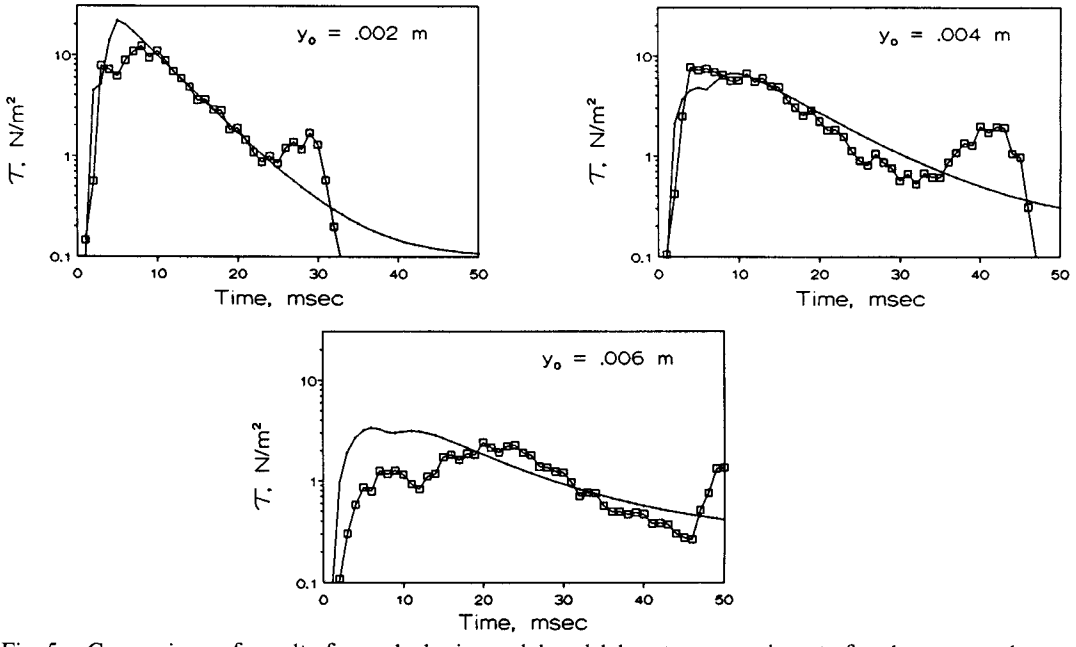

Fig. 5. Comparison of results from algebraic model and laboratory experiments for three water layer depths.

Comparaison des résultats du modèle algébrique et des mesures expérimentales pour trois profondeurs d'écoulement.

Fig. 6 illustrates the agreement between the model and the measured data with respect to the effect of distance from the center of drop impact. The series of graphs clearly shows that both the model and the measured data indicate an order of magnitude reduction in boundary shear stress for a distance of .010 m as compared with .005 m.
Additionally, both model and experimental data indicate that the effect of the drop is nonexistent at a distance of .015 m.

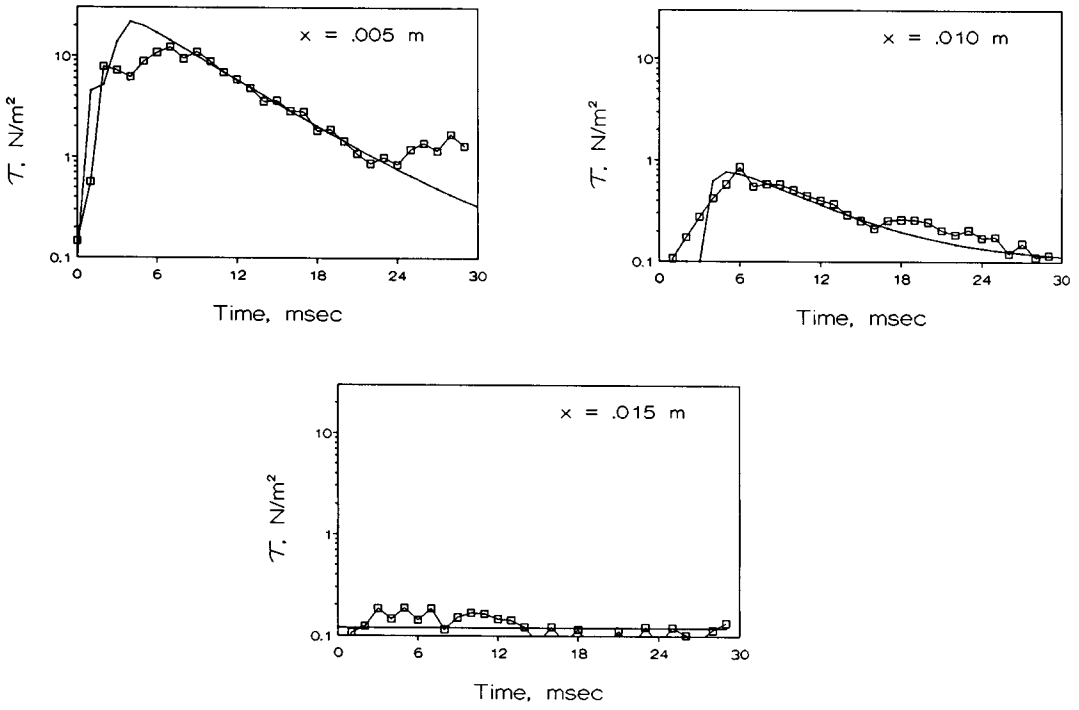

Fig. 6. Comparison of results from algebraic model and laboratory experiments for three radial distances.
Compariason des résultats du modèle algébrique et des mesures expérimentales à trois distances radiales.

A comparison of results for three different drop impact velocites is shown in Fig. 7. For the first graph ($V_0 = 1.0$ m/s), the match between model and experimental data appears quite good during the initial 15 msec. However, at later times, measured boundary shear stress values exceed predicted ones. This may result from the entrainment of air bubbles during the collapse of the splash crater which can cause the hot-film probe to register an erroneously high boundary shear stress readings. This effect is not evident in the other two graphs in the figure because the higher impact velocities extend the period of splash crater expansion. At the intermediate drop impact velocity, both the simulated and measured boundary shear stress peaks are larger than at the lowest impact velocity, however, the simulated value is about half as large as the measured one. At the largest impact velocity, both peaks again exhibit an increase over peaks at the intermediate value; however, in this case the simulated value is larger than the measured value. Thus, in this

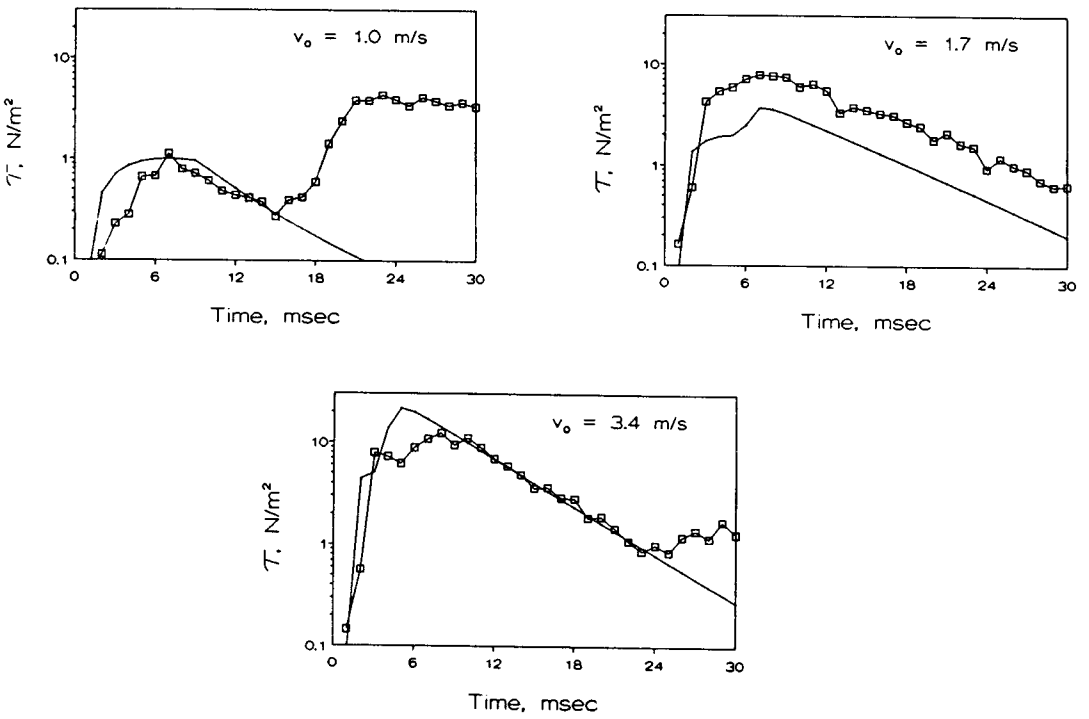

Fig. 7. Comparison of results from algebraic model and laboratory experiments for three impact velocities.
Comparaison des résultats du modèle algébrique et des mesures expérimentales pour trois vitesses de chute.

set of comparisons, the model and measured data display the same trend with respect to impact velocity if only the initial measured boundary shear stress pulse is considered.

Fig. 8 presents a comparison of measured and simulated results for three different drop diameters. Although peak values of the simulated pulses are somewhat higher than measured peaks, the trend toward larger peak boundary shear stresses at larger drop sizes is evident in both the measured and simulated results. Additionally, boundary shear stress pulse durations of the simulated and measured pulses are quite similar.

Fig. 9 represents a summary comparison of all 150 experimentally measured peak boundary shear stresses with model estimates. Although there is scatter about the line of perfect agreement, the model estimates peak boundary shear stresses which are within a factor of 2.0 of the measured values for about 79% of the data. The model appears to underestimate peak boundary shear stresses for conditions which produce small values i.e. large flow depths and small impact velocities. However, these are of less practical interest than larger values. For peak boundary shear stresses greater than 1.0 N/m^2, the number of estimates which are within a factor of two of the measured values rises to 85%.

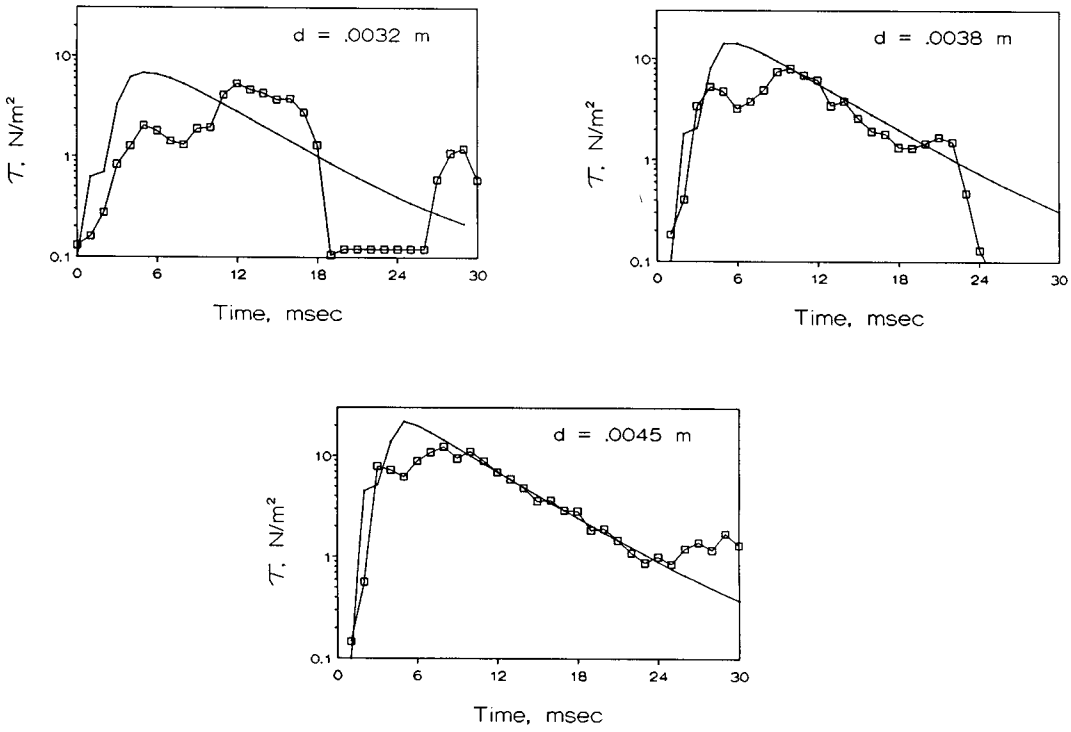

Fig. 8. Comparison of results from algebraic model and laboratory experiments for three raindrop sizes.
Comparaison des ré
mètres de gouttes.

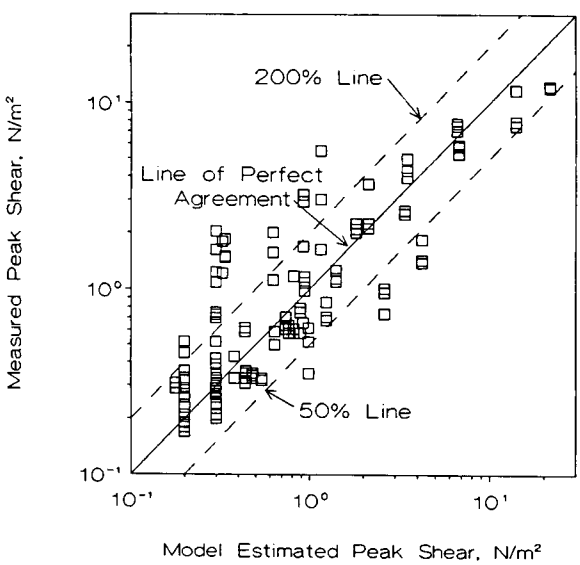

Fig. 9. Comparison of peak shear estimates from algebraic equations with measured values for all experimental runs.

Comparaison des pointes de cisaillement tirées des équations algébriques avec les valeurs mesurées pour toutes les expériences.

7 Summary and conclusions

A set of dimensionless algebraic equations which approximately describe the boundary shear stress field induced by raindrop impact during the period of splash crater expansion has been developed. The independent variables in these equations were derived from physical reasoning and dimensional analysis and their specific functional forms were developed empirically using data generated from a series of numerical experiments. The numerical model used to generate these data utilizes a finite difference solution to the equations of two-dimensional motion for a viscous, incompressible fluid, with a free surface. Excellent agreement between the simplified algebraic model and the numerical model is demonstrated over a wide range of values of the specified, dimensionless, independent variables.

Subsequently, the algebraic relationships were validated using laboratory experiments involving a range of drop sizes, impact velocities and water layer depths. For the shallowest depths investigated in the experiments, peak boundary shear stresses in excess of 10 N/m^2 were measured and duly estimated by the algebraic model. Given the larger impact velocities and smaller depths which may exist under natural rainfall conditions, maximum peak boundary shear stresses may be 5 to 10 times as great as the largest values measured in the experiments.

Results of this study indicate that the magnitude of the dimensionless boundary shear stress is strongly and inversely dependent on the dimensionless depth and also to a lesser extent inversely dependent on the drop Reynolds number. Gravity and surface tension forces appear to exert a minor influence in the generation of large boundary shear stresses caused by raindrops impacting shallow layers of water. However, these forces tend to affect the boundary shear stress field as the fluid decelerates and the boundary shear stress magnitudes decay. The spatial distribution of the boundary shear stress at any time during the crater expension period can be estimate by a beta distribution. The parameters of the distribution are functions of the dimensionless variables defined in the analysis.

This study focused on the boundary shear stress caused by a single, isolated raindrop. Knowledge gained concerning the spatial and temporal scales of the shear field should be useful in analysing the degree of raindrop interaction under natural rainfall conditions. However, if independence of raindrops is assumed, the algebraic relationships developed in this study provide a convenient and efficient first approximation for the magnitude, spatial extent and duration of boundary shear stresses caused by rainfall on overland flow. The determination of these boundary shear stress distributions represents an important component in the mathematical modeling of soil detachment and sediment transport from upland surfaces.

Acknowledgment

The authors wish to thank Dr. Donn Decoursey and Dr. Carlos Alonso of the United States Department of Agriculture Research Service for their support and assistance throughout the course of this study. The experiments were carried out at the Hydraulic Laboratory of the Engineering Research Center of Colorado State University.

Notations

Symbol[1/2]

A	coefficient in probe calibration equation
B	constant in probe calibration equation, $(M/LT^2)^{1/3}$
C_1	correction factor in dimensionless maximum peak boundary shear stress equation
C_2	correction factor in equation for dimensionless time to reach maximum peak shear stress
C_β	beta function coefficient
d	drop diameter, L
E	anemometer output- electrical potential, $L^2M/(T^3I)$
F	drop Froude number
g	gravitational acceleration, L/T^2
$p1$	first power of beta function
$p2$	second power of beta function
$p1_d$	first power of beta function during decay period
$p2_d$	second power of beta function during decay period
R	drop Reynolds number
R_e	base flow Reynolds number
r	radius of drop
S	channel friction slope
t	point in time after drop impact, T
t^*	dimensionless time after drop impact
t^{**}	dimensionless time scaled by dimensionless time to reach maximum peak boundary shear stress
$t^*_{p\,max}$	dimensionless time to reach maximum peak boundary shear stress
V_0	drop impact velocity, L/T
V_x	base flow velocity, L/T
W	drop Weber number
x	distance from center of drop impact
x^*	dimensionless distance from center of drop impact, L
x^*_p	dimensionless position of peak boundary shear stress
x^*_{pd}	dimensionless position of peak boundary shear stress during boundary shear decay
x^*_r	dimensionless right boundary of beta function
x^*_{rd}	dimensionless right boundary of beta function during boundary shear stress decay
y	vertical space coordinate and flow depth, L
y_0	water layer depth, L
y^*_0	dimensionless water layer depth
ϱ	fluid density, M/L^3
σ	surface tension, M/T^2
ν	kinematic viscosity, L^2/T
γ	specific weight of fluid, $M/(T^2L^2)$
θ	combined gravity and surface tension parameter
τ	boundary shear stress, $M/(LT^2)$

[1] M = mass, L = length, T = time, I = unit of electrical current.
[2] (boundary shear stress dimensions)$^{1/3}$/(electrical potential dimensions)^2

τ^* dimensionless boundary shear stress

τ_p peak boundary shear stress, $M/(LT^2)$

τ_p^{**} dimensionless peak boundary shear stress scaled by dimensionless maximum peak boundary shear stress

$\tau_{p\,max}$ maximum peak boundary shear stress, $M/(LT^2)$

$\tau_{p\,max}^*$ dimensionless maximum peak boundary shear stress

λ gamma functional parameter

λ_d Exponential decay parameter

References / Bibliography

DeCoursey, D. G. and Snyder, W. M. (1969), Computer-oriented method of optimizing hydrologic model parameters, Journal of Hydrology, 9, pp. 34–56.

Engel, O. G. (1966), Crater depth in fluid impacts, Journal of Applied Physics 37(4), pp. 1798–1808.

Harlow, F. H. and Shannon, J. P. (1967), The splash of a liquid drop, Journal of Applied Physics, 38(10), pp. 3855–3866.

Hartley, D. M. (1990), Boundary shear stress induced by raindrop impact, Ph.D. dissertation, Dept of Civ. Engr., Colorado State Univ., Fort Collins, 193 pp.

Hartley, D. M. and Alonso, C. V. (1991), Numerical study of maximum boundary shear stress induced by raindrop impact, Water Resources Research 27(8), pp. 1819–1826.

Hirt, C. W. and Nichols B. D. (1981), Volume of fluid (VOF) method for the dynamics of free boundaries, Journal of Computational Physics, 39, pp. 210–225.

Hobbs, P. V. and Kezweeny, A. J. (1967), Splashing of a water drop, Science 155, pp. 1112–1114.

Hobbs, P. V. and Osheroff, T. (1977), Splashing of drops on shallow liquids, Science 158, pp. 1184–1186.

Huang, C., Bradford, J. M. and Cushman, J. M. (1982), A numerical study of raindrop impact phenomena, SSSA Journal 46, pp. 14–20.

Laws, J. O. (1939), Short exposure photographs of water-drops striking soil, U.S. Department of Agriculture, Soil Conservation Service, 12 pp.

Laws, J. O. (1940), Recent studies of raindrops and erosion. Agricultural Engeneering, 21, p. 431.

Macklin, W. C. and Hobbs, P. V. (1969), Subsurface phenomena and splashing of drops on shallow liquids, Science 166, pp. 107–108.

Macklin, W. C. and Metaxes, G. J. (1976), Splashing of drops on liquid layers, Journal of Applied Physics 47(9), pp. 3963–3969.

Mutchler, C. M. and Hansen, L. M. (1970), Splash of a waterdrop at terminal velocity, Science 169, pp. 1311–1312.

Mutchler, C. M. and Young, R. A. (1975), Soil detachment by raindrops, In: Present and Prospective Technology for Predicting Sediment Yields and Sources, U.S. Department of Agriculture, Agricultural Research Service, ARS-S-40, pp. 113–117.

Nichols, B. D., Hirt, C. W. and Hotchkiss, R. S. (1980), SOLA-VOF, A solution algorithm for transient fluid flow with multiple free boundaries, Report LA-8355, Los Alamos Scientific Laboratory, 119 pp.

Rajaratnam, N. (1976), Turbulent jets, (Developments in water science; 5), American Elsevier, New York.

Sandborn, V. A. (1972), Resistance and temperature transducers, Metrology Press, Fort Collins, 545 pp.

Schall. J. D. (1979), Spatial and time distribution of boundary shear stress in open channel flows, M.S. thesis, Department of Civil Engineering, Colorado State University, Fort Collins, Colorado, 156 pp.

Tan, S. (1990), Rainfall and soil detachment, Journal of Hydraulic Research, 27(5), pp. 699–715.

Wang, R. C. (1970), The mechanics of a drop after striking a stagnant water layer, Ph.D. dissertation, Dept. Civ. Eng., Univ. of Illinois, Urbana, 131 pp.

Welch, J. E., Harlow, F. H. Shannon, J. P. and Daly, B. J. (1965), The MAC method: a computing technique for solving viscous, incompressible, transient fluid-flow problems involving free surfaces, Report LA-3425, Los Alamos Scientific Laboratory, Los Alamos, New Mexico, 146 pp.

Worthington, A. M. (1882), On impact with a liquid surface. Proceedings of the Royal Society (London), 32, p. 217.

Worthington, A. M. (1908), A study of Splashes, Longmans, Green and Co.

Worthington, A. M. (1963), A Study of Splashes, MacMillan, New York.